Accessing the Potential of Bismuth Oxide Nanosheets for an incredible revelation in the removal of contamination in water bodies

**Mohammed Kuku[1], Sultan Althahban[1] and Yosef Jazaa[2,3]**

[1]Department of Mechanical Engineering, Jazan University, Jazan 82822, Saudi Arabia.

[2]Department of Mechanical Engineering, College of Engineering, King Khalid University, P.O. Box 394, Abha 61421, Saudi Arabia.

[3]Center for Engineering and Technology Innovations, King Khalid University, Abha 61421, Saudi Arabia.

*to whom all correspondence should be addressed: e-mail: mkuku@jazanu.edu.sa

GRAPHICAL ABSTRACT
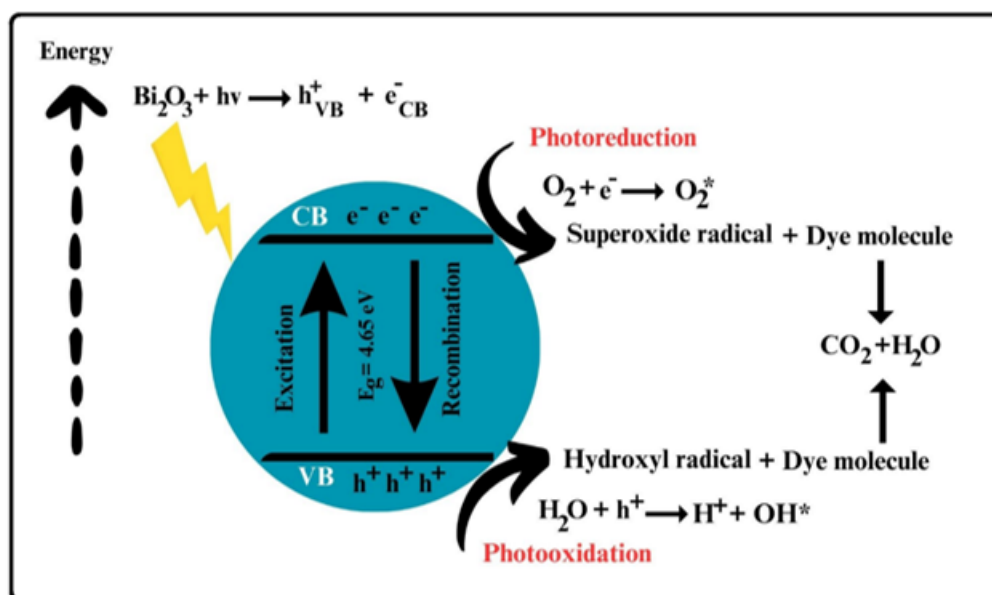
Abstract

Water contamination is a pressing global issue with far-reaching environmental, health, and socio-economic consequences. As the demand for clean water intensifies, researchers are exploring innovative nanomaterials to develop efficient and sustainable water treatment technologies. The Bismuth oxide (Bi_2O_3) nanosheets were synthesized using a sustainable approach comprising Moringa oleifera seed extract as a biological capping and reducing agent. Analytical techniques were utilized to inspect the prepared nanosheets' crystalline, morphological, and optical characteristics. The optical properties, including light absorption and bandgap width were investigated at the bandgap energy of 4.65 eV. In addition, the nanosheet's ability to degrade cationic malachite green and Rhodamine 6G dye and anionic eosin yellow and reactive black dyes by photocatalysis was evaluated. The degradation of cationic and anionic dyes was characterized by nanocatalysis through pseudo-first-order kinetics prototypical. The pseudo-first-order degradation kinetic rate of malachite green and Rhodamine 6G was determined to be 3.46 and 3.20 X 10^{-2} min^{-1}, indicating that the prepared

nanosheets effectively initiate this dye's degradation. The results showed dye degradation was more effective at cationic dyes than anionic dyes.

1.   Introduction

The utilization of nanoparticles offers multiple advantages in diverse sectors and contexts (Tomchenko et al, 2003). Nanomaterials generally exhibit a significant surface area-to-volume ratio due to their small size at the nanoscale. Because of this feature, their reactivity is increased, and as a result, they are ideally suited for applications such as catalysis and sensing. Nanocatalysts have superior catalytic activity and efficiency in comparison to their macroscopic counterparts. This approach confers benefits in several industrial applications, such as chemical synthesis and environmental remediation. In recent times, there has been increasing research attention to the sustainable production of nanomaterials by utilizing environmentally responsible techniques (Li et al, 2016).

The utilization of green synthesis techniques depends on the intrinsic characteristics of natural sources to generate nanoparticles, facilitating the advancement of environmentally sustainable and highly effective nanomaterials (Huan-Wen et al, 2010). Green synthesis often involves using natural extracts or biomolecules, making the resulting nanomaterials more biocompatible and safer for the environment and human health. These methods frequently utilize renewable resources, such as plant extracts or biomass, reducing dependence on non-renewable raw materials and contributing to sustainability. Green synthesis methods are often more energy-efficient compared to traditional chemical methods. They tend to generate less waste compared to conventional chemical methods. Using precise reaction conditions and avoiding unnecessary reagents contribute to reducing waste production (Sijakovic-Vujicic et al, 2004). In some cases, green synthesis methods can be more cost-effective. Using readily available natural resources and eliminating expensive or hazardous reagents contribute to cost savings. It is often easily scalable, allowing for the production of nanomaterials on a larger scale without significantly modifying the process. Additionally, optimizing green synthesis processes is an ongoing area of research to enhance their efficiency and applicability further (Dhage et al, 2003). *Moringa oleifera* is a multifaceted botanical specimen that has garnered attention due to its diverse range of health advantages and sustainable utility. The seeds of the *Moringa* plant are known for their abundance of bioactive substances, making them highly sought after in industries such as medicine, nutrition, and nanomaterial creation. Bioactive chemicals in *Moringa oleifera* seeds have been linked to several therapeutic benefits. The benefits encompassed in this category consist of anti-inflammatory, antioxidant, antibacterial, and anti-diabetic properties (Fang et al. 2017). The extract has historically been employed across different cultures in holistic health. The seed extract of *Moringa oleifera* possesses inherent coagulant activities. Traditionally, it has been conventionally used in water purification, functioning as a naturally occurring flocculant that aids in water purification by eliminating pollutants and sediment. The utilization of *Moringa oleifera* seed extract in the fabrication of nanomaterials by the guidelines of green chemistry provides a sustainable substitute for conventional synthesis techniques that employ

aggressive chemicals. *Moringa oleifera* seed extract has attracted considerable interest due to its abundant bioactive chemical content, which can function as both reducing and stabilizing agents during nanomaterial fabrication. The conventional approaches to nanoparticle synthesis frequently require potentially harmful chemicals and energy-intensive procedures, increasing environmental apprehensions (Li et al, 2017). Green synthesis methods aim to mitigate these concerns by utilizing natural extracts that are readily available, renewable and have negligible ecological consequences. The utilization of *Moringa oleifera* seed extract, which possesses favorable biocompatibility and a high concentration of phytochemical compounds, follows the principles of green synthesis. This encompasses synthesizing metal oxide nanoparticles, with particular attention on synthesizing bismuth oxide nanosheets. Bismuth-based materials have garnered significant interest owing to their cost-effective and sustainable characteristics. The low toxicity of bismuth and related derivatives and its biocompatibility and ease of manufacture have contributed to this attention. Significant applications in various electronic devices. Different crystalline forms of bismuth oxide have been identified, together with α-Bi_2O_3, β- Bi_2O_3, γ- Bi_2O_3, δ- Bi_2O_3, ϵ- Bi_2O_3, and ω- Bi_2O_3, which are determined by variations in temperature.

The compound Bi_2O_3 has garnered significant interest due to its diverse range of applications. Bi_2O_3 exhibits inactivity when exposed to neutral water and possesses a bandgap energy inside the visible area, precisely measuring 2.8eV. It can oxidize water, generating highly reactive species that initiate oxidation reactions. This property makes it suitable for degrading dyes, gases, and pharmaceuticals in chemistry (Masui et al, 2006). Bismuth oxide (Bi_2O_3) has attracted considerable interest in photocatalysis due to its distinctive characteristics, such as a suitable bandgap, substantial surface area, and remarkable photocatalytic performance when exposed to visible light. Photocatalysis uses materials such as bismuth oxide to absorb light energy, create electron-hole pairs, and engage in redox reactions to facilitate various operations. Photocatalysis is a chemical process in which a catalyst, activated by light, accelerates a reaction without being consumed. The key to photocatalysis is using a material known as a photocatalyst, which can absorb light and then use that energy to drive chemical reactions. This field has gained significant attention for its potential applications in various industries, including environmental remediation, energy production, and synthesis of valuable chemicals. Bismuth oxide photocatalysts have effectively broken-down organic pollutants in air and water environments (Sudrajat et al, 2017). This application holds particular significance within the scope of environmental remediation. Efficient photocatalysis requires minimizing the rewiring of electron-hole pairs, which can reduce the quantum efficiency of the process. Strategies to inhibit recombination include co-catalysts and surface modifications (Raut et al, 2017). Here, to the best of our knowledge, there is a shortage of published literature that comprehensively summarizes the utilization of bio-synthesized bismuth-based photocatalysts for water treatment. This research aims to assess the properties of *M. oleifera* seeds with Bi_2O_3 nanosheets for photocatalytic applications. The physicochemical properties of *Moringa oleifera* seeds (MOS) extract-mediated synthesized Bi_2O_3 nanosheets were evaluated using several characterization techniques and catalytic properties for photocatalytic applications. The synthesized Bi_2O_3 nanosheets were studied for their application in photocatalytic degradation

of cationic (Rhodamine 6G and Malachite green) and anionic (Eosin yellow and Reactive black) dyes under Sunlight irradiation (Nurmalasari et al, 2020).

2. Materials and methods

The Bismuth nitrate ($Bi(NO_3)_3$) and ethanol were procured commercially from Sigma-Aldrich, Himedia, and Merck, respectively. An aqueous extract was made from *Moringa oleifera* seeds acting as a reducing mediator during the synthesis of Bi_2O_3 nanosheets. The seeds were procured from the Namakkal region in Tamil Nadu, India.

2.1. Green synthesis of Bi₂O₃

Initially, *Moringa oleifera* seeds were crushed into small pieces and subjected to a drying by exposing to sunlight after thorough washing using distilled water. To prepare the extract, 20 grams of *Moringa oleifera* seeds were immersed in 200mL of distilled and deionized water (DD water) at 80°C for 2 hrs. The acquired seed extract was cooled to apartment temperature and filtered via Whatman strainers (Zhang et al, 2008). For the preparation of bismuth oxide nanoparticles through green synthesis, 100 mL of *Moringa oleifera* seeds extract was added with 0.1 molar concentration (equivalent to 2.9 grams) of bismuth nitrate precursor. The resulting solution was subjected to sonication for 30 minutes at 40 Hz. Subsequently, the heterogeneous solution underwent agitation for 24 hours at a consistent rotational speed, then placed in a heated air oven for the night. The dry powders underwent five rounds of centrifugation with DD and ethanol to eliminate visibly detectable chemical substances. Subsequently, the samples were dried at 80°C. Following this, the samples underwent calcination for 3 hours at a temperature of 400°C within a muffle furnace (Poorsajadi et al, 2022) (Figure 1).
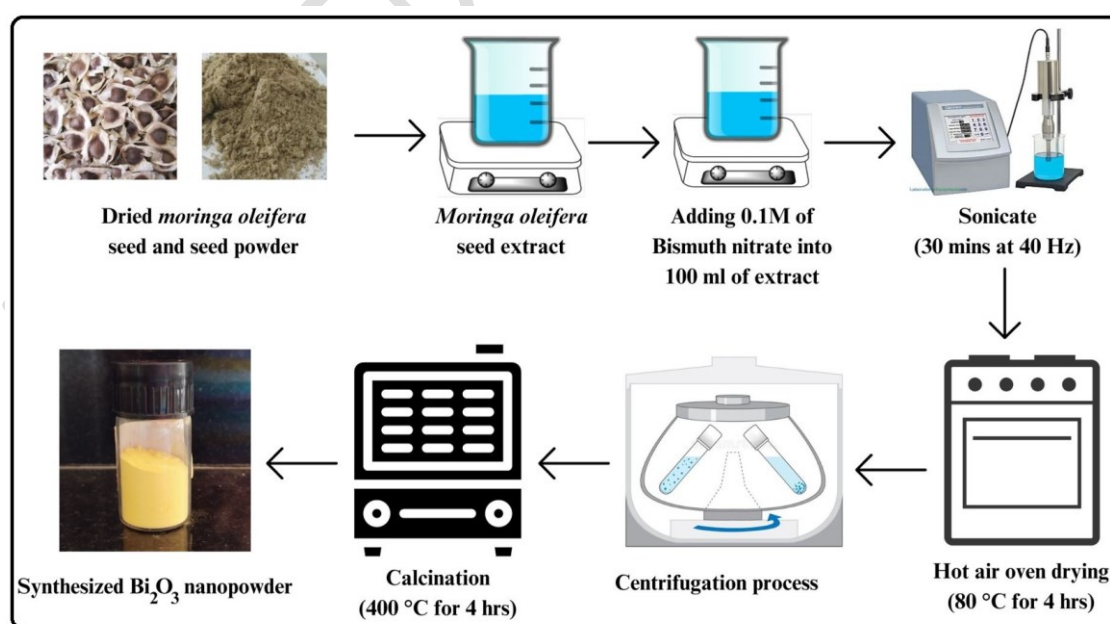

Figure 1. The Bi_2O_3 nanoparticle synthesis

2.2. Preparation of aqueous dye for photocatalytic activity

Under sunlight illumination, the photocatalytic activity of Bi_2O_3 nanosheets was studied for degrading cationic (Malachite green and Rhodamine 6G) and anionic (Eosin yellow and Reactive black) dyes in an aqueous solution. The study focused on the photocatalytic activity of the nanosheets. The dyes were diluted to a standard amount, and 20 mg of Bi_2O_3 nanosheets was introduced into the aqueous dye solution following the photocatalytic degradation technique. The photoreaction was conducted using annular UV irradiation in a cubic UV reaction chamber. A UV lamp with a power output 40W and a dominant emission wavelength was employed to irradiate at the outer edges of the UV reactor (Agilent, Singapore). At regular intervals of 30 minutes, a volume of 5 ml of the aqueous solution was extracted from the illuminated region to measure the UV absorbance range of the dyes (Tian et al, 2003) and the photocatalytic degradation efficiency (%) was determined using equation (1).

$$\text{Dye degradation efficiency } \eta = \frac{C_o - C_t}{C_o} X \ 100 \ \% \tag{1}$$

Equation (1) represents the calculation of η, expressed as a percentage, where η is determined by subtracting C_t from C_0 and dividing the result by C_0, then multiplying by 100. The degradation percentage, denoted as η, is defined as the ratio of the decrease in absorbance of a dye, represented by C_t to its original absorbance, described by C_0.

2.3. Characterization of Bi_2O_3 nanosheets

The X-ray diffractometry was used to evaluate the phase clarity and assess the prepared Bi_2O_3 nanosheets' structural components. The polycrystalline phase, lattice parameters, functional group identification, average particle size, optical absorbance & bandgap of Bi_2O_3 nanosheets were estimated through XRD, FULLPROF software, FTIR, light scattering technique, UV-Vis spectroscopy (180 to 800 nm), respectively. Surface topology and morphological characteristics of Bi_2O_3 nanosheets were considered using SEM and EDX through elemental mapping analysis. Further, photoluminescence spectroscopy was used to explore the electronic and optical possessions of Bi_2O_3 nanosheets.

3.   Results and discussion

The XRD investigations were steered to ascertain the characteristics of polycrystalline phase and the interplanar spacing. The sharp peak found at 28° with lattice parameters of a = b = 7.739 Å, c = 5.636 Å for all diffraction peaks (JCPDS: 27-0050) and a space collection P421C (114) emphasis the β- Bi_2O_3. The `d' values and relative concentrations are enumerated in Table 1. The Figure 3 confirms the XRD patterns of Bi_2O_3 nanosheets, which display peaks at 27.8°, 30.8°, 33.1°, 45.4°, 47°, 52.9°, 55.8° and 57.2° equivalent to the crystalline planes (201), (002), (220), (222), (400), (203), (421) and (402), correspondingly. The existence of a distinct diffraction peak provides evidence for the high degree of crystallinity shown by Bi_2O_3 nanosheets. The average Crystalline size 'd' was calculated through Scherrer equivalence (Equation 2) (Tian et al, 2003).
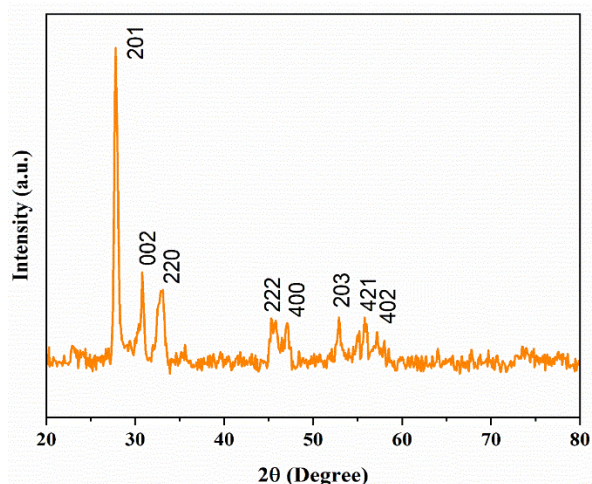
$$d = \frac{k\lambda}{\beta cos\theta} \tag{2}$$

Figure 2. XRD pattern for prepared Bi_2O_3 nanopowder

The average crystalline size of Bi_2O_3 NPs was estimated as 21.4 nm. Furthermore, the Rietveld refinement technique assessed the degree of agreement between the calculated and observed The X-ray diffraction (XRD) pattern. The Rietveld refinement was conducted with the Fullprof analytical program, employing the JCPDs card no. 27 - 0050 as the reference pattern (Figure 3). The crystal structure is observed to be tetragonal, with a space group indexed as P421C (114). Using the Thompson-Cox-Hastings pseudo-Voigt distribution, an initial refinement was carried out in order to guarantee that the pattern fit was suitable. The axial divergence asymmetry peak form parameter and a polynomial function with six coefficients were both subjected to analysis as part of this effort (Oudghiri-Hassani et al, 2015).

Table 1. The `d' values and relative intensities.

Miller indices	2theta (degree)	FWHM (degree)	Crystal size (nm)	d-spacing (nm)	Dislocation density in 1/nm^2
(201)	27.8	0.48	17.80766	0.32	0.003153
(002)	30.8	0.38	22.64836	0.28	0.00195
(220)	33.1	0.87	9.949393	0.27	0.010102
(222)	45.4	0.38	23.66859	0.2	0.001785
(400)	47	0.38	23.80998	0.19	0.001764
(203)	52.9	0.38	24.38804	0.17	0.001681
(421)	55.8	0.38	24.70698	0.16	0.001638
(402)	57.2	0.38	24.86971	0.16	0.001617
		Average	**21.48109**		**0.002961**

The functional group of Bi_2O_3 nanosheet was determined by FT-IR and depicted in the Figure 5. The absorption peaks found at 1385 cm^{-1} are ascribed to the vibrational mode of C-O, while the 3438 cm^{-1} peak indicates the stretching of -OH groups in Bi_2O_3 nanosheet. The 700 ~ 400 cm^{-1} spectral band is attributed to the vibration of metal-oxygen (Bi-O) at a wavenumber of 477 cm^{-1}. The C-O vibration was observed at the wavenumber of 1385 cm^{-1} and stretching vibration of C-H bond at 2927 cm^{-1} provides evidence of flavonoid compounds' existence.
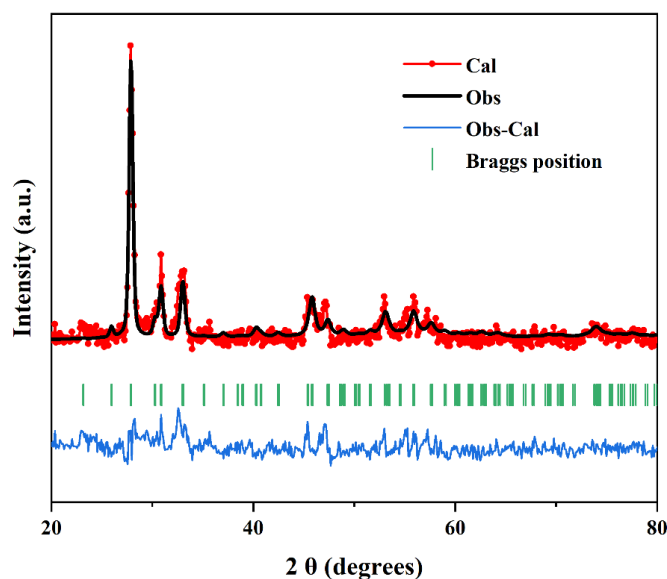
Figure 3. Rietveld refinement of prepared Bi_2O_3 nanosheet.

The existence of saponin may be determined from the vibrational frequency of the C=O group at 1637 cm^{-1}, while the presence of alkaloids detected from the stretching vibration of C-N at 1097 cm^{-1}. The vibrational mode observed at a wavenumber of 2853 cm^{-1} indicates C-H stretching (Popa et al, 1998). Furthermore, several parameters, including background, peak shape parameters, atom location, scale factors, and lattice functions, were revised to match the estimated data satisfactorily. According to the results presented in the Table 1, the revised lattice parameters of the prepared Bi_2O_3 nanosheets, as obtained from the refinement data, are as follows: a = b = 7.739 Å, and c = 5.636 Å. The refinement parameters, including Rp, Rwp, Rexp, and Chi2 values, obtained from Table 2 confirm that the analysed samples are devoid of further impurities and agree with the estimated XRD patterns. The refinement results corroborate the earlier research findings, providing evidence that the synthesized materials' structural integrity has not been significantly altered.

Table 2. Crystallographic characteristics of Bi_2O_3 nanosheets

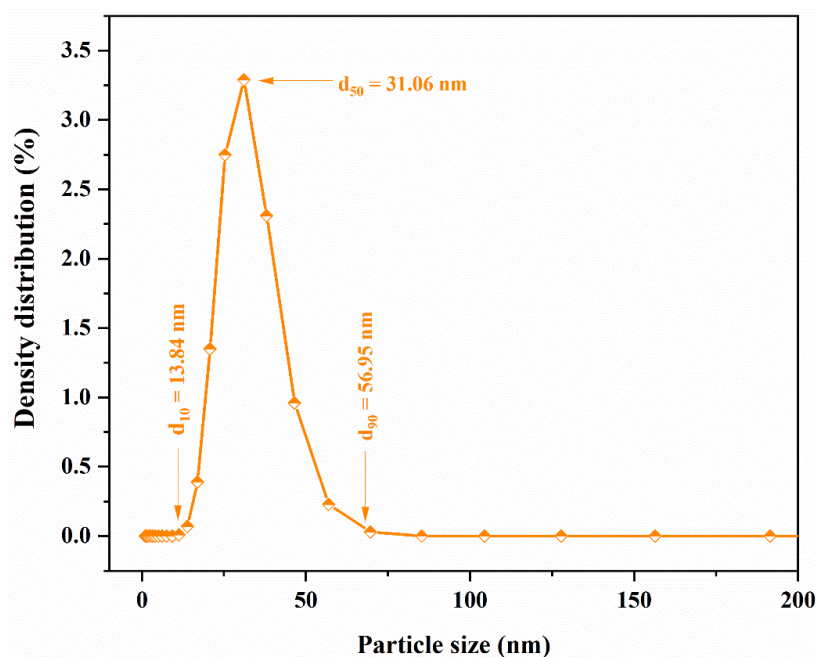| Sample	:	Bi_2O_3
Average size (nm)	:	21.4
Lattice parameters (Å)	:	a = b = 7.739 Å
		c = 5.636 Å
Cell volume (nm^3)	:	33.7
Rp	:	10.3
Rwp	:	12.7
Rexp	:	8.11
Chi square (χ^2)	:	1.4

Figure 4. Particle size analysis for Bi_2O_3 nanosheet

The size and dispersion ability of Bi_2O_3 nanosheet are exposed in the Figure 4. The prepared nanosheet's particle size is determined using the dynamic light scattering principle. Bi_2O_3 nanosheet' particle size distribution is 13.84 nm (d10) to 56.5 nm (d90). The average particle size (d50) is 31.06 nm, respectively. The UV-Visible (UV-Vis) spectroscopy is a significant analytical technique employed to investigate electronic transitions in molecules, including nanoparticles. Figure 6 demonstrates the equivalent UV-Vis absorption spectra of Bi_2O_3 nanosheet and it exhibits a distinct absorption peak at a wavelength of 267 nm, which can be attributed to the presence of Bi_2O_3. The UV range of 267 nm acquired corresponds to the absorption peak or band observed in the UV-Vis spectra.
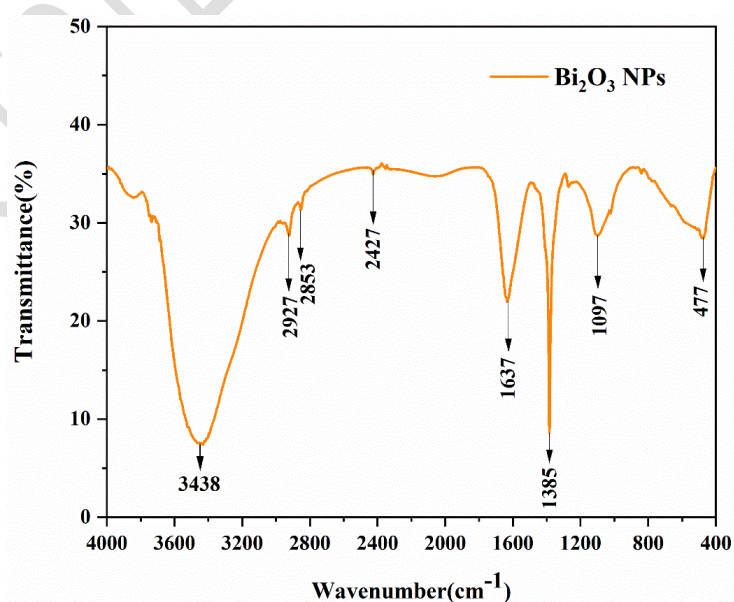

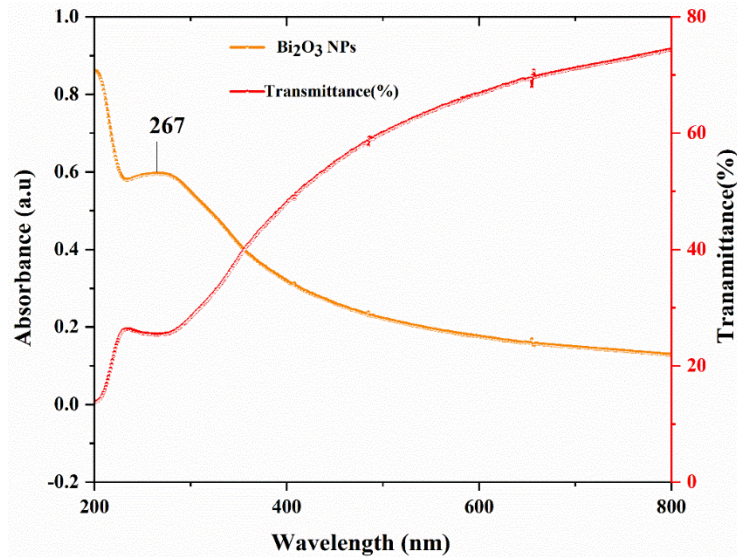**Figure 5.** FTIR spectra of Bi_2O_3 nanosheet

Figure 6. UV-visible spectra of Bi_2O_3 nanosheets

The observed absorption phenomenon is commonly attributed to electronic transitions involving the nanoparticles' valence electrons. The optical characteristics of nanoparticles can be influenced by their size (Eberl et al, 2008). When it comes to nanoparticles, the phenomenon of quantum size effects is becoming more and more relevant, which leads to dramatic changes in the absorption spectrum. Surface plasmon resonance is another factor that has the potential to influence the absorption peak. This is especially true in situations when the nanoparticles have different surface features. When Moringa oleifera seed extract is used into the synthesis process, there is a possibility that organic ligands or functional groups will be embedded into the surface of the nanoparticles. In addition to having the ability to impact the electrical structure, organic components may also contribute to the reported absorption characteristics (Schlesinger et al, 2013). The Tauc equation was used to determine the band gap of Bi_2O_3 nanosheet.

$$\alpha(\upsilon)h = K(h\upsilon - Eg)^n \qquad (3)$$

In the provided formula, K represents a constant, Eg the energy band gap, ϕ the frequency, h the Planck constant, and α the absorption coefficient. Figure 7 displays the square of the variable in relation to the energy variable h. Where the absorption edge-created tangent line extends to intersect the energy axis is a good indicator of the band gap size. Consequently, approximating the absorption peak at 267 nm, the predicted bandgap energy is around 4.65 eV. So, in this case, when the bandgap energy is 4.65 eV, the trend towards shorter wavelengths indicates the presence of relatively small nanoparticles. Based on these results, it seems that quantum confinement has an effect on the electrical structure. At the specific wavelength of 267 nm, the transmittance of Bi_2O_3 nanosheets denotes the proportion of incident light that passes through the sample without being absorbed. Ideally, the transmittance value at 267 nm would be expressed as a percentage, indicating the percentage of light transmitted through the sample at that specific wavelength (Liu et al 2013).
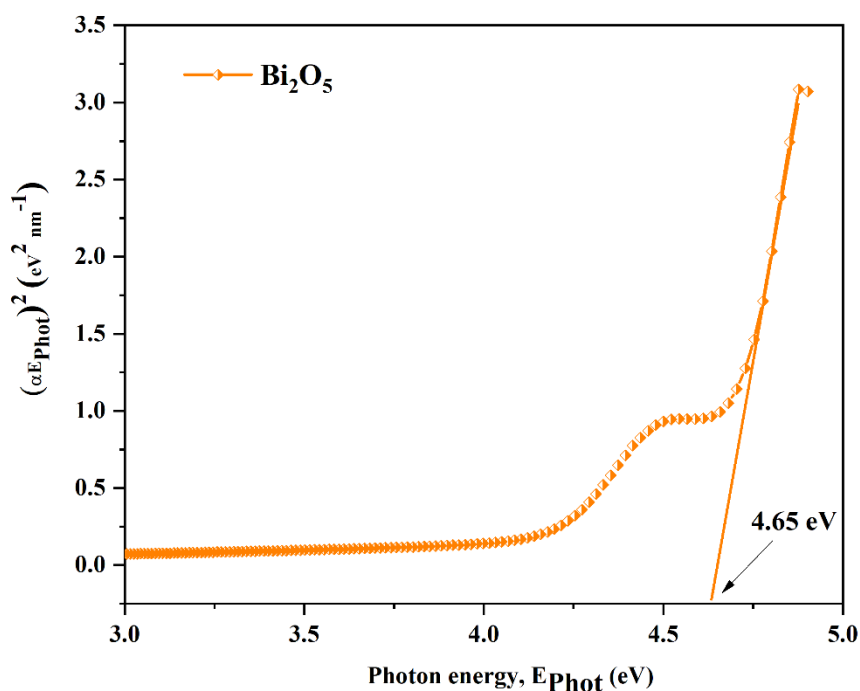
Figure 7. Tauc plot of Bi_2O_3 nanosheets

The morphology analysis was conducted using a SEM, and images were captured at various magnifications. At low magnifications (figure 8 a), the SEM images revealed the overall morphology of the bismuth oxide nanosheets. The nanosheets had a distinct, well-defined, two-dimensional structure with a high aspect ratio. The sheets appeared to be interconnected, forming a network of nanoscale structures. Upon increasing the magnification [figure 8 (b and c)], finer details of the nanosheet morphology became apparent. The edges of the nanosheets appeared smooth, indicating a well-defined crystalline structure. Some nanosheets displayed a slight curvature, suggesting flexibility or a degree of structural adaptability. The nanostructures' purity was assessed using the EDX approach as shown in Figure 8 (d). The purity of the product is apparent, as demonstrated by the presence of distinct peaks corresponding to the elements Bi and O. These peaks exhibit an average atomic percentage ratio of 86.82% of O and 13.18% of Bi, respectively. The elemental analysis provides evidence of the existence of the respective elements in non-stoichiometric proportions. Figure 9 shows the TEM images of prepared Bi_2O_3 nanosheets. TEM imaging reveals the Bi_2O_3 nanosheets displayed a two-dimensional morphology with an extended and planar structure. It shows the finer details of the nanosheet structure. The edges of the nanosheets appeared sharp and well-defined, indicating a high level of crystallinity. The layer-by-layer arrangement of atoms within the nanosheets was discernible, highlighting the material's two-dimensional nature (Yang et al, 2019).
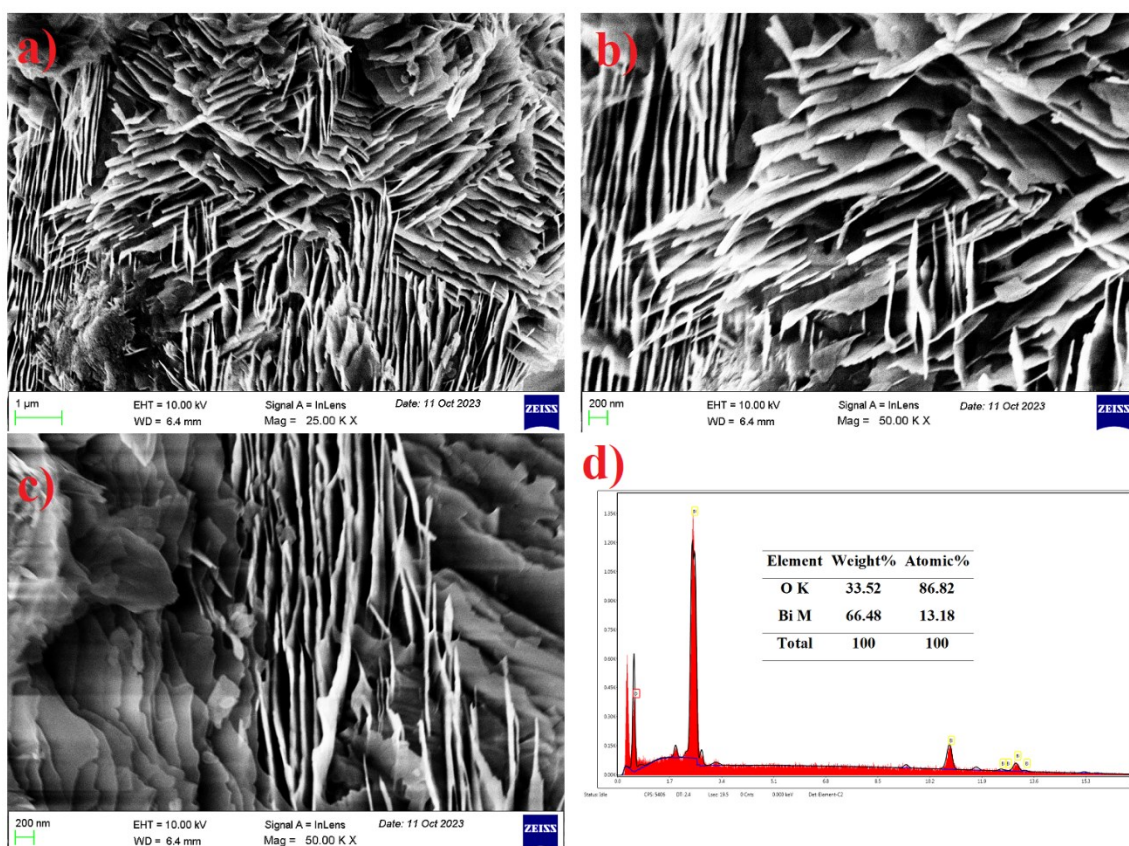
Figure 8. Morphology analysis (a, b, and c), EDAX (d) of Bi_2O_3 nanosheets

The SAED pattern is shown in Figure 9 (d). The SAED analysis was conducted to probe the crystallographic orientation of the Bi_2O_3 nanosheets. A selected area on the nanosheet-covered grid was chosen for electron diffraction. The obtained SAED pattern exhibited diffraction rings consistent with the two-dimensional nature of the nanosheets. The pattern revealed distinct diffraction spots corresponding to specific crystallographic planes of Bi_2O_3. The presence of concentric rings indicated the polycrystalline nature of the nanosheets, with the diffraction providing information about the arrangement of atoms within the individual crystallites. Analysis of the SAED pattern allowed for the determination of crystallographic data, such as lattice spacing and orientation of the nanosheets (Fang et al, 2011). The catalytic activity of Bi_2O_3 nanosheets under Sunlight irradiation as model pollutants dyes cationic (Rhodamine 6G and malachite green) and anionic (reactive black and eosin yellow) dyes are employed. These model dyes mimic the physical and chemical properties of certain pollutants, such as heavy metals or organic compounds. They provide a way to observe and track the movement of contaminants in water systems without the risks associated with actual pollutants. The efficacy of the nanomaterial in the degradation of dye is assessed at regular 15-minute intervals. The whole process is prolonged to a duration of 90 minutes in order to achieve optimal degrading effectiveness of contaminants by the nanomaterials. Bismuth oxide nanosheets exhibit remarkable photocatalytic activity under both ultraviolet (UV) and visible light. This property enables them to harness solar energy for catalysing chemical reactions that degrade organic pollutants, presenting a sustainable and energy-efficient water treatment approach.
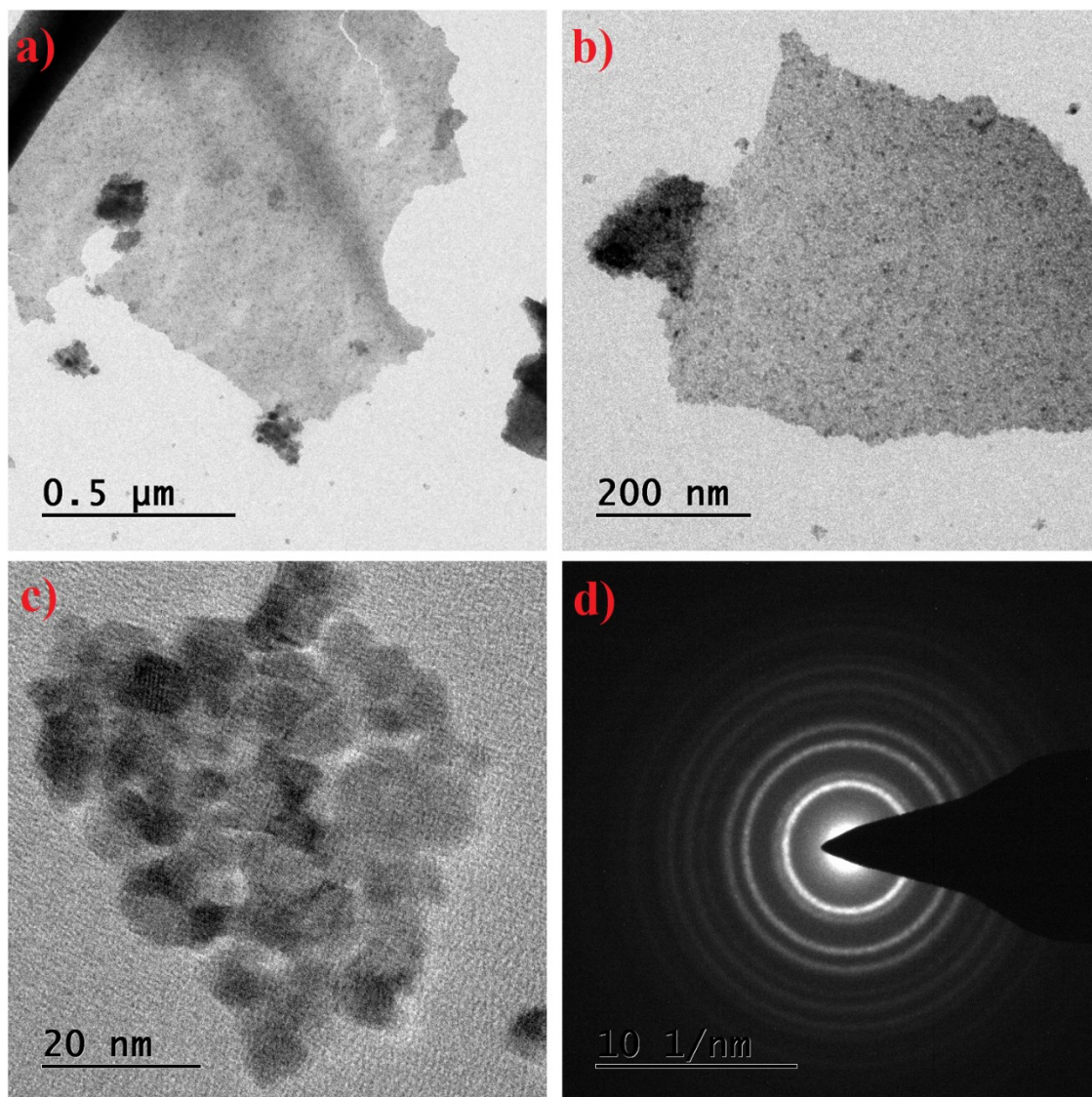
Figure 9. TEM image of prepared Bi_2O_3 nanosheet

The reduction in the absorbance of the dye was seen as the duration of light irradiation increased, as shown in Figure 10. The decrease in absorbance observed presents strong evidence for the efficient degradation of the dyes aided by the created samples when exposed to visible-light irradiation and the photocatalytic degradation efficiency are estimated through the Equation 4 (Zhang et al, 2008).

$$Dye\ Degradation\ efficiency = \frac{(D_0 - D_t)}{D_0}\ \% \tag{4}$$
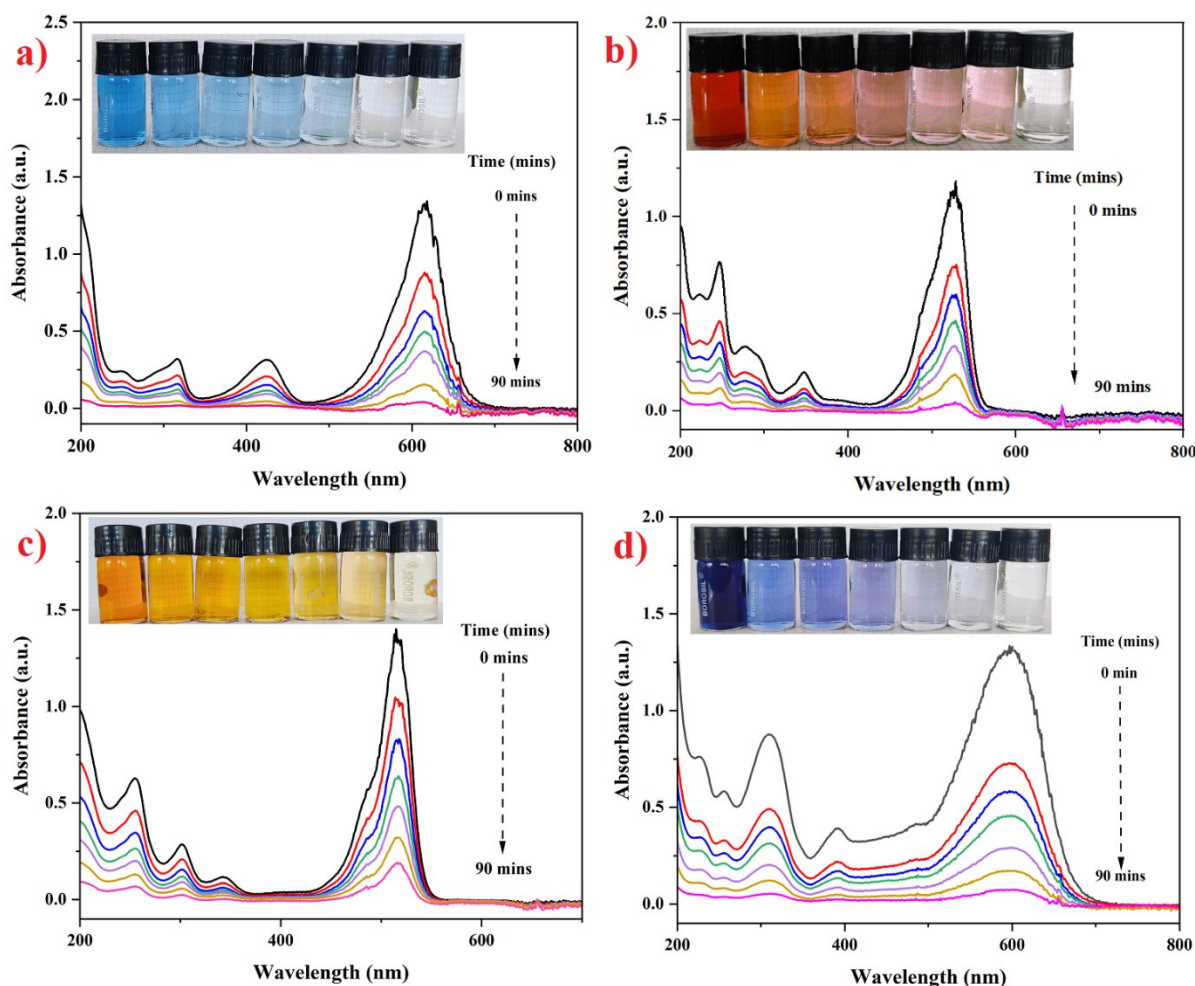
Figure 10. Absorbance-dye degradation graph of cationic dyes: a) MG, b) Rh 6G;
Anionic dyes: c) EY, d) RB

The time-dependent degradation efficacy of Cationic dyes is 96.5% and 97%, respectively, for Rhodamine 6G and malachite green dye. Similarly, for anionic dyes is about 94.4% and 86.1%, respectively, for reactive black and eosin yellow dyes, shown in figure 13. This implies that the nanocatalyst facilitates the process of self-degradation of dye molecules (Chakrabarti et al, 2004). Anionic dyes have a much lesser capacity for colour gradation when contrasted with cationic dyes. The nanoparticle is a better location for dye adsorption because it is enriched in phytochemical species of Moringa oleifera seeds. The determined photocatalytic degradation efficiency is shown graphically in Figure 3. Several things could be responsible for the enhanced photocatalytic performance. The photocatalytic activity of nanosheets is enhanced due to their reduced optical bandgap. To evaluate the rate of degradation of the synthetic samples, a first-order kinetic model was used (Zhang et al, 2008).

$$\ln\left(\frac{c}{c_0}\right) = -\mathrm{k}t \qquad (5)$$

Table 3. Photocatalyst with dye degradation rate constant

Name of the Photocatalyst	Name of the Dye	Concentration (mg/L)	Kinetic rate constant (x 10^{-2} min^{-1})	Efficiency (%)

	MG	10	3.46	97.04
Bi$_2$O$_3$	Rh6G		3.20	96.5
	EY	10	2.09	86.1
	RB		2.92	94.4

Figure 11 shows the C/C0 curve, which shows the concentration fluctuations seen in the presence of dye solutions loaded with nanocatalysis and in the absence of catalyst. Here we can see the graph representing the decline in dye molecular number over a period of 90 minutes.
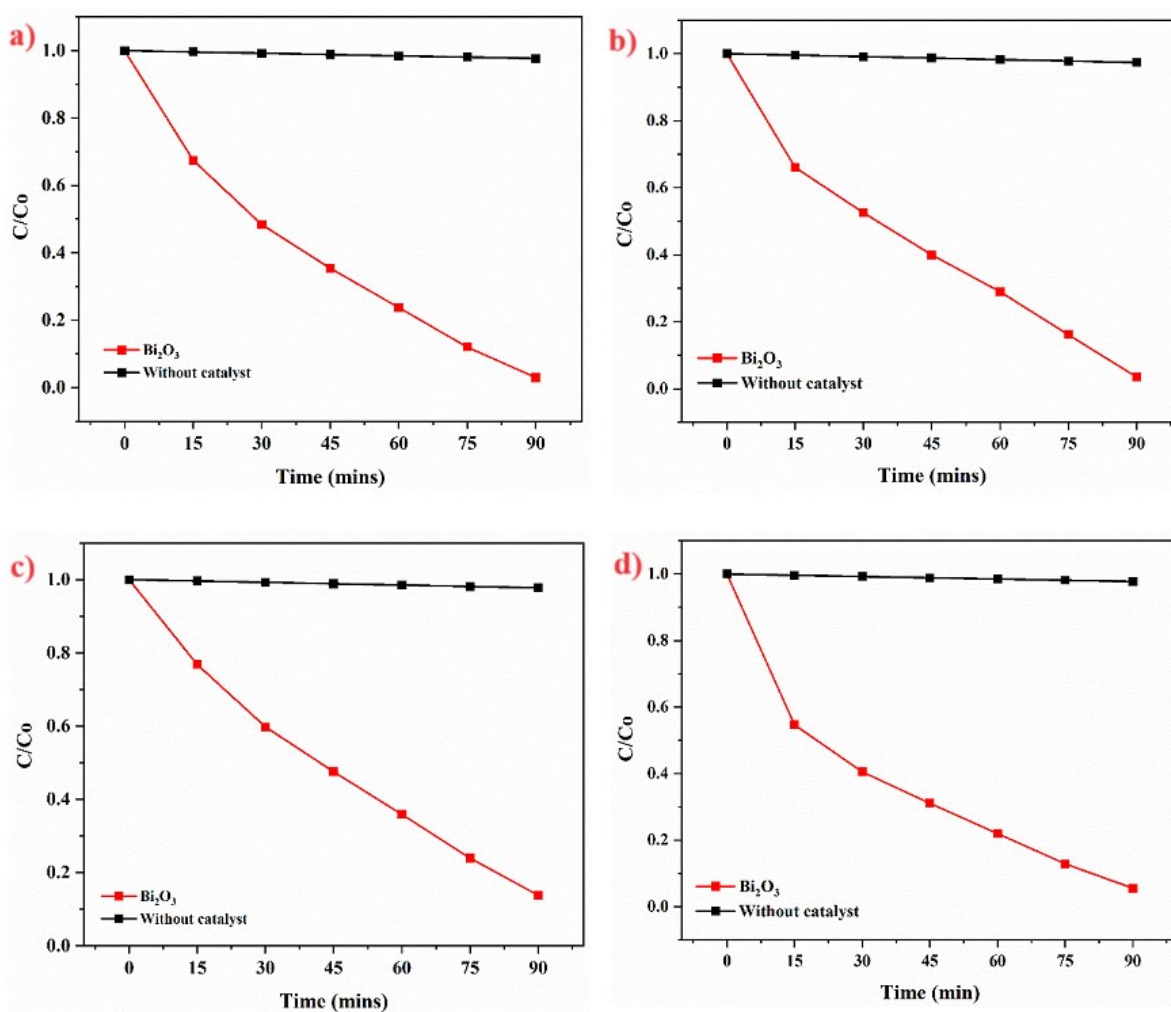

Figure 11. C/C0 curves for cationic dyes: a) MG, b) Rh 6G; Anionic dyes: c) EY, d) RB

As described by Figures 11 and 12 and tabulated in Table 3, the calculated kinetic parameters for the synthesized Bi$_2$O$_3$ nanosheets with the degradation of cationic Rh6G and MG dyes are 3.20×10^{-2} min^{-1} and 3.46×10^{-2} min^{-1} respectively. Similarly, the kinetic values for the anionic RB and EY dyes are 2.92×10^{-2} and 2.09×10^{-2} min^{-1}, respectively. The cationic dyes have a significantly higher degradation rate than anionic dyes, with an estimated increase of 1.7 times. The increased degradation rate may be attributed to the reduced bandgap, possibly due to the enriched phytochemical species of *Moringa oleifera* seeds. The band gap effectively reduces the coalesce of electron-hole pairs and it leads to the increased absorption of photons for excitation and charge separation. The transmission of electrons from the nanoparticle to the

14

adsorbed dye molecules induces a redox breakdown (Zhang et al, 2008). The formation of reactive oxygen species is made possible by the photocatalytic characteristics of bismuth oxide nanosheets, which allow for the destruction of organic contaminants.
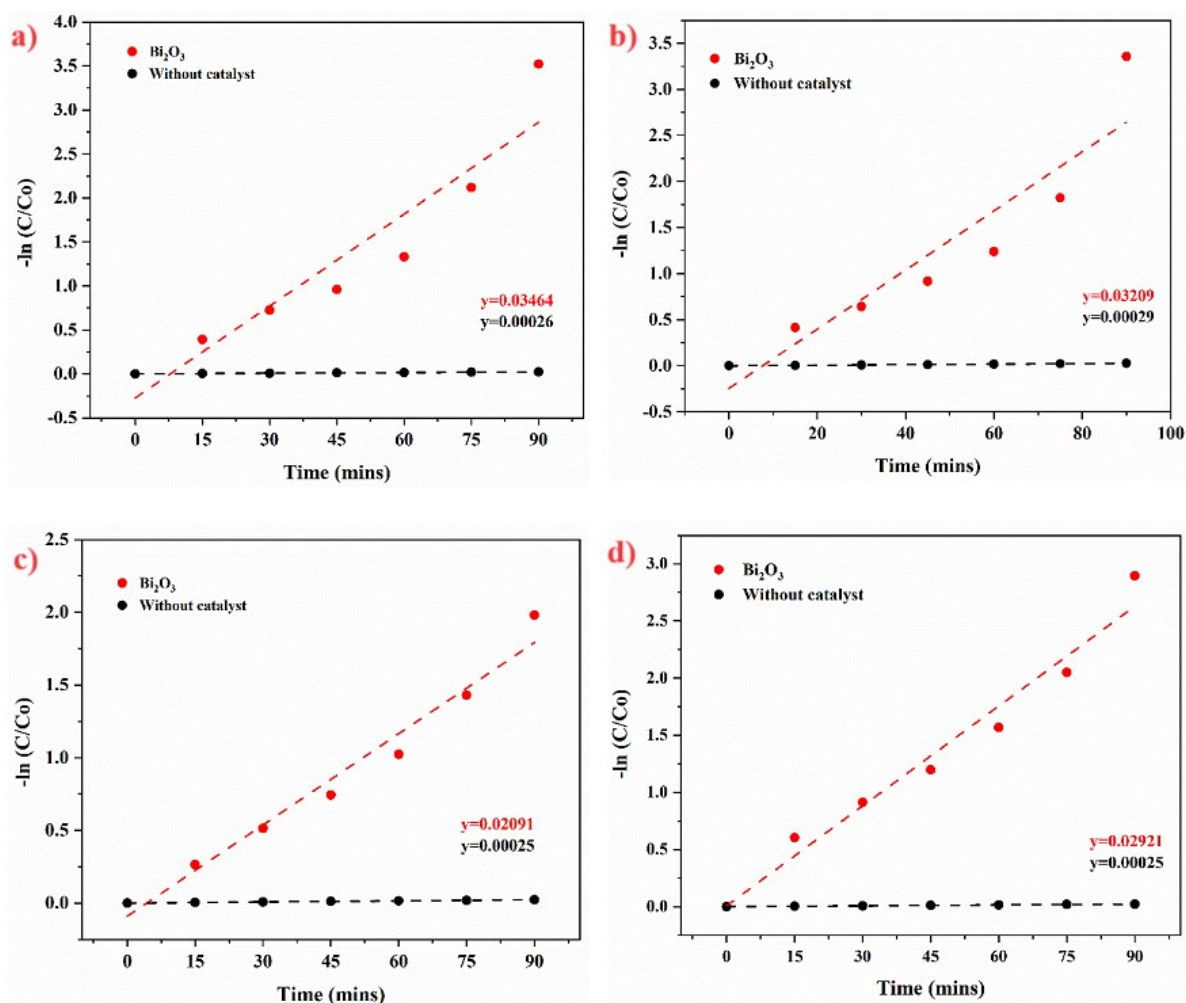

Figure 12. Pseudo-first-order degradation kinetics for cationic dyes: a) MG, b) Rh 6G; Anionic dyes: c) EY, d) RB

The selective adsorption capacity of bismuth oxide nanosheets can be tailored for specific contaminants. This customization makes them versatile for addressing diverse water quality challenges and allows for the design of targeted water treatment strategies. Therefore, the photoactive behavior of the Bi_2O_3 nanosheets can be observed during the degradation of cationic and anionic dyes, including reactive black and eosin yellow. The process of dye degradation by photocatalysis may be performed through either direct or indirect methods. Decomposition occurs through the direct pathway, which involves the photosensitization of dyes by the absorption of photons. Consequently, dissolved oxygen decreases, leading to superoxide radical ions (O_2^-) forming, which undergo additional reactions to generate highly reactive hydroxyl radicals (OH). As mentioned above, radicals are crucial in initiating the degradation processes. The process of decomposition occurs indirectly through the in-situ formation of electron-hole pairs. When semiconductor catalyst particles are subjected to radiation with an energy level denoted as (hv), empirical observations have shown that the

energy of the radiation (hv) is either equivalent to or above the band gap energy (Eg) of such particles. Following this, the electrons in the conduction band (CB) decrease compounds that receive electrons, such as dissolved O_2 in the solution, resulting in the creation of O_2- ions.
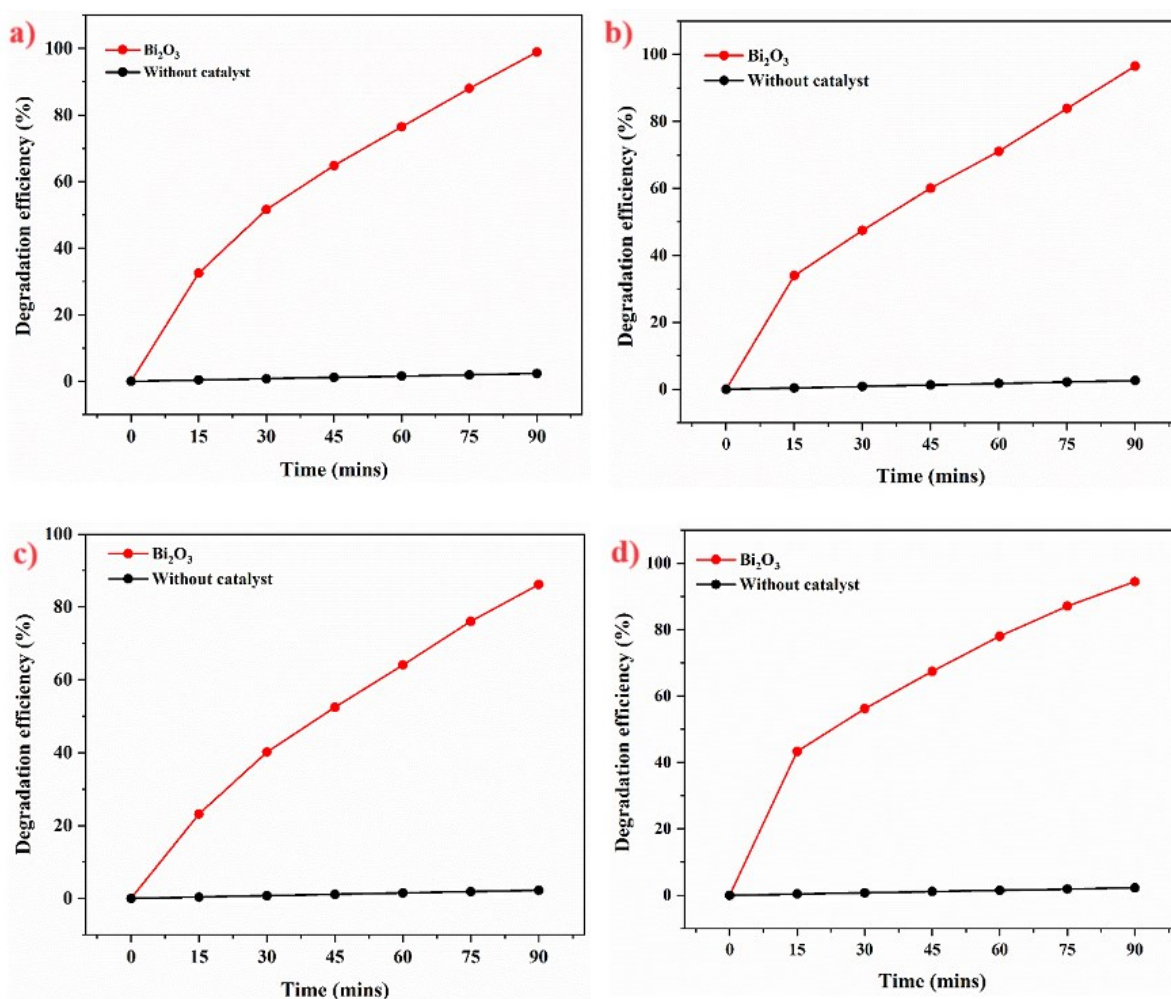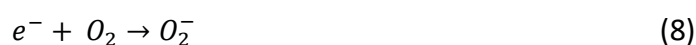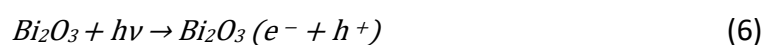

Figure 13. Bi_2O_3 nanosheet degradation efficiencies against cationic dyes: a) MG, b) Rh 6G; Anionic dyes: c) EY, d) RB

The valence band (VB) holes enable the oxidation process of electron-donating species, such as H_2O, to the production of OH radicals. Following this, decomposition begins with forming intermediate compounds, producing ecologically benign chemicals, namely carbon dioxide (CO_2), water (H_2O), and a small number of mineral acids. It has been shown that the indirect approach, out of the two available decomposition methods, has superior kinetic velocity and functions as the principal pathway for the degradation of organic pollutants. The following equations provide significant insight into the potential process behind dye degradation by the synthesized nanosheet.

$$Bi_2O_3 + hv \rightarrow Bi_2O_3 \ (e^- + h^+) \tag{6}$$

$$h^+ + H_2O \rightarrow H^+ + OH^- \tag{7}$$

$$e^- + O_2 \rightarrow O_2^- \tag{8}$$

16

$$O_2^- + H^+ \rightarrow HO_2 \tag{9}$$

$$\textit{Dye molecules} + *HO + O_2- \rightarrow \textit{Degraded products}\,(CO_2 + H_2O) \tag{10}$$

The probable mechanism of photocatalytic degradation for the synthesized materials is shown in Figure 14. The degrading process of Bi_2O_3 nanosheet is characterized by a significant photocatalytic activity, which is attributed to the absorption of photons. Such substances are present in several chemical processes, including hydroxylation, dehydrogenation, and oxidative cleavage of dye functional groups. These processes disintegrate dye molecules, yielding smaller and less complex byproducts. Simultaneously, dye molecules undergo adsorption onto the catalyst's surface via physical interactions, increasing the proximity to the active sites (Zhang et al, 2008). The photocatalytic process persists through the continuous regeneration of photogenerated charge carriers due to their absorption of additional photons. This enables the catalyst to sustain its catalytic activity throughout time. Hence, due to electrostatic attraction, negatively charged Bi_2O_3 particles enhance the adsorption of positively charged dye molecules (RhB and MG), resulting in a higher dye adsorption capacity than anionic dyes (RB and EY) (Zhang et al, 2008).
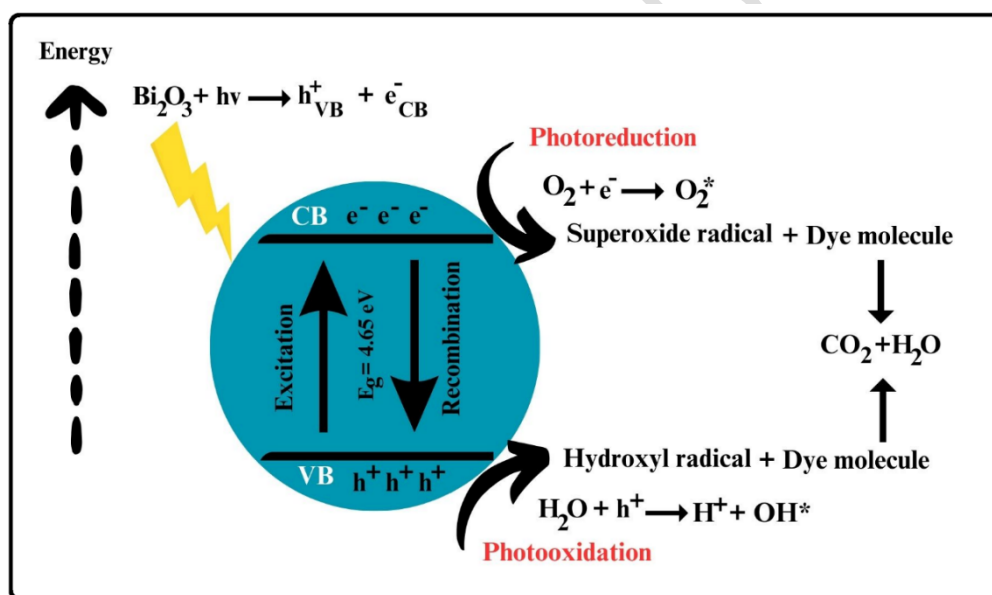

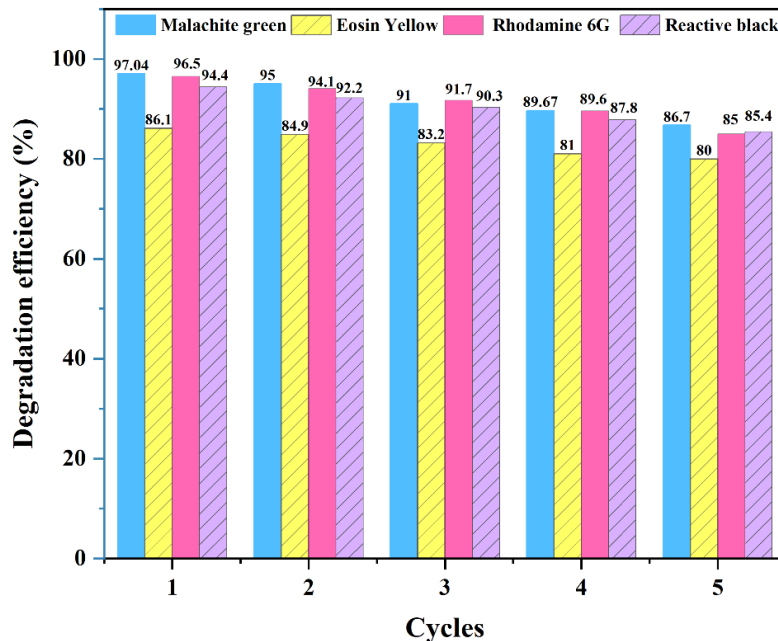**Figure 14.** Degradation mechanism for prepared Bi_2O_3 nanosheet

Figure 15. Recycling studies of Bi_2O_3 nanosheets

The analysis of the reusability and stability of the photocatalyst has significant economic implications. Hence, the present study aimed to observe the stability of the photocatalyst and explore the potential for reusing Bi_2O_3 catalysts, and the bar graph has been represented in Figure 15. Following each phase, the catalyst underwent a process of reconstitution, washing, and drying in an oven, thereby enabling its reuse. The experiment was conducted across four cycles, as depicted in Figure 15. The degradation percentages of cationic Malachite green dyes decreased from 97.04% to 86.7%, and Rhodamine 6G dye decreased from 96.5% in the initial stage to 85% in the final step. Moreover, anionic eosin yellow dye decreased from 86.1% at the initial stage to 80% in the final stage, and reactive black dye decreased from 94.4% in the initial step to 85.4% in the final stage. As a result, the nanosheet demonstrates excellent stability in the degradation of organic dyes. After four reuse cycles, the ICP-OES measurement showed that just 3% of the nanosheet had disintegrated. Since the generated nanosheet's photocatalytic activity is little diminished, it demonstrates exceptional stability in this regard.

4.   Conclusion

The greatest effectiveness of degrading anionic dyes (Rh 6G) and cationic dyes (MG) by Bi_2O_3 nanosheets in an aqueous solution was observed as 97.04% and 96.50%, respectively, after 90 minutes of exposure to visible light. The occurrences might be explained by the increased surface area of the sheets and the decreased probability of charge-carrier recombination. Both the MG and Rh6G dye photodegradation rate constants 3.46 and 3.20 $X10^{-2}$ min^{-1}, respectively were determined to be in the presence of Bi_2O_3 nanosheets. Furthermore, the generated nanosheet exhibits remarkable stability in photocatalytic activities, as shown by the little decrease in activity. The potential of Bi_2O_3 nanosheets as a long-term, efficient means of filtering out harmful substances from water has us hopeful for a water future free of pollution.

18

References

Chakrabarti S. and Dutta B.K. (2004). Photocatalytic Degradation of Model Textile Dyes in Wastewater Using ZnO as Semiconductor Catalyst, *Journal of Hazardous Materials,* 112, 269–278.

Dhage S.R., Pasricha R. and Ravi V. (2003). Synthesis of Ultrafine TiO_2 by Citrate Gel Method, *Materials Research Bulletin, 38*, 1623–1628.

Eberl J. and Kisch H. (2008). Visible Light Photo-Oxidations in the Presence of α-Bi_2O_3, *Photochemical & Photobiological Sciences, 7*, 1400–1406.

Fang G., Chen G., Wang X. and Liu J. (2011). Synthesis and Luminescence of Single Crystalline Bi_2O_3 Nanosheets, *Science China Technological Sciences, 54*, 19–22.

Fang W., Fan L., Zhang Y., Zhang Q., Yin Y., Zhang N. and Sun K. (2017). Synthesis of Carbon Coated Bi_2O_3 Nanocomposite Anode for Sodium-Ion Batteries, *Ceramics International, 43*, 8819–8823.

Huan-Wen W., Zhong-Ai H., Yan-Qin C., Yan-Li C., Zi-Qiang L., Zi-Yu Z. and Yu-Ying Y. (2010). Facile solvothermal synthesis of a graphene nanosheet–bismuth oxide composite and its electrochemical characteristics, *Electrochimica Acta,* 55, 8974-8980.

Li L., Meng L., Wang F. and Wang Y. (2017). Synthesis and Optical Characterization of In3+-Stabilized γ-Bi2O3 Sillenite Semiconductor with Cation Deficiency. *Materials Science in Semiconductor Processing*, 68, 48-52.

Li L., Xitian Z., Zhiguo Z., Mingyi Z., Lujia C., Yu P. and Shuangyan L. (2016). A bismuth oxide nanosheet-coated electrospun carbon nanofiber film: a free-standing negative electrode for flexible asymmetric supercapacitors, *Journal of Materials Chemistry A*, 4, 16635-16644.

Liu H., Luo M., Hu J., Zhou T., Chen R. and Li J. (2013). β-Bi_2O_3 and Er^{3+} Doped β-Bi_2O_3 Single Crystalline Nanosheets with Exposed Reactive {001} Facets and Enhanced Photocatalytic Performance, *Applied Catalysis B: Environment and Energy, 140-141*, 141–150.

Masui T., Furukawa S. and Imanaka N. (2006). Synthesis and Characterization of CeO_2–ZrO_2–Bi_2O_3 Solid Solutions for Environment-Friendly Yellow Pigments, *Chemistry Letters, 35*, 1032–1033.

Nurmalasari N., Yulizar Y. and Apriandanu D.O.B. (2020). Bi_2O_3 Nanoparticles: Synthesis, Characterizations, and Photocatalytic Activity, *Materials Science and Engineering, 763*, 012036.

Oudghiri-Hassani H., Rakass S., Al Wadaani F.T., Al-ghamdi K.J., Omer A., Messali M. and Abboudi M. (2015). Synthesis, Characterization and Photocatalytic Activity of α-Bi_2O_3 Nanoparticles, *Journal of Taibah University for Science, 9*, 508–512.

Poorsajadi F., Sayadi M.H., Hajiani M. and Rezaei M.R. (2022). Synthesis of CuO/Bi_2O_3 Nanocomposite for Efficient and Recycling Photodegradation of Methylene Blue Dye, *International Journal of Environmental Analytical Chemistry, 102*, 7165–7178.

Popa M., Ţoţovãnã, A., Popescu L., Drãgan N. and Zaharescu M. (1998). Reactivity of the Bi, Sr, Ca, Cu Oxalate Powders Used in BSCCO Preparation, *Journal of the European Ceramic Society, 18*, 1265–1271.

Raut S.S., Bisen O. and Sankapal B.R. (2017). Synthesis of Interconnected Needle-like Bi$_2$O$_3$ Using Successive Ionic Layer Adsorption and Reaction towards Supercapacitor Application, *Ionics, 23*, 1831–1837.

Schlesinger M., Weber M., Schulze S., Hietschold M. and Mehring M. (2013). Metastable β-Bi$_2$O$_3$ Nanoparticles with Potential for Photocatalytic Water Purification Using Visible Light Irradiation, *ChemistryOpen, 2*, 146–155.

Sijakovic-Vujicic N., Gotic M., Music S., Ivanda M. and Popovic S. (2004). Synthesis and Microstructural Properties of Fe-TiO$_2$ Nanocrystalline Particles Obtained by a Modified Sol-Gel Method, *Journal of Sol-Gel Science and Technology. 30*, 5–19.

Sudrajat H. and Sujaridworakun P. (2017). Low-Temperature Synthesis of δ-Bi2O3 Hierarchical Nanostructures Composed of Ultrathin Nanosheets for Efficient Photocatalysis, *Materials & Design*, *130*, 501–511.

Tian Z.R., Voigt J.A., Liu J., McKenzie B., McDermott M.J., Rodriguez M.A., Konishi H. and Xu H. (2003). Complex and Oriented ZnO Nanostructures, *Nature Materials*, *2*, 821–826.

Tomchenko A.A., Harmer G.P., Marquis B.T. and Allen J.W. (2003). Semiconducting Metal Oxide Sensor Array for the Selective Detection of Combustion Gases, *Sensors and Actuators B, 93*, 126–134.

Yang J., Wang M., Zhao S., Liu Y., Zhang W., Wu B. and Liu, Q. (2019). Biotemplate Preparation of Bi$_2$O$_3$ Nanosheet for Enhanced Photodegradation of Methylene Blue, *Micro & Nano Letters, 14*, 705–710.

Zhang J., Shi F., Lin J., Chen D., Gao J., Huang Z., Ding X. and Tang C. (2008). Self-Assembled 3-D Architectures of BiOBr as a Visible Light-Driven Photocatalyst, *Chemistry of Materials*, *20*, 2937–2941.

Zhang J., Xu Q., Feng Z., Li M. and Li C. (2008). Importance of the Relationship between Surface Phases and Photocatalytic Activity of TiO$_2$, *Angewandte Chemie International Edition, 47*, 1766–1769.